

Vibrational properties of LiNbO₃ and LiTaO₃ under uniaxial stress

Ekta Singh^{*,1,*} Mike N. Pionteck^{*,2,†} Sven Reitzig,¹ Michael Lange,¹ Michael Rüsing,¹ Lukas M. Eng,^{1,3} and Simone Sanna²

¹*Institut für Angewandte Physik, Technische Universität Dresden, 01062 Dresden, Germany*

²*Institut für Theoretische Physik and Center for Materials Research (LaMa), Justus-Liebig-Universität Gießen, 35392 Gießen, Germany*

³*ct.qmat: Dresden-Würzburg Cluster of Excellence—EXC 2147, TU Dresden, 01062 Dresden, Germany*

(Dated: October 26, 2022)

Structural strain severely impacts material properties such as the linear and non-linear optical response. Moreover, strain plays a key role, e.g., in the physics of ferroelectrics and in particular of their domain walls. μ -Raman spectroscopy is a well-suited technique for the investigation of such strain effects, as it allows to measure the lattice dynamics locally. However, quantifying and reconstructing strain fields from Raman maps requires knowledge on the strain dependence of phonon frequencies. In this work, we have analyzed both theoretically and experimentally the phonon frequencies in the widely used ferroelectrics lithium niobate and lithium tantalate as a function of uniaxial strain via density functional theory and μ -Raman spectroscopy. Overall, we find a good agreement between our *ab initio* models and the experimental data performed with a stress cell. The majority of phonons show an increase in frequency under compressive strain, while the opposite is observed for tensile strains. Moreover, for E-type phonons, we observe the lifting of degeneracy already at moderate strain fields (i.e. at $\pm 0.2\%$) along the x and y directions. This work hence allows for the systematic analysis of 3D strains in modern-type bulk and thin-film devices assembled from lithium niobate and tantalate.

Keywords: Lithium niobate, lithium tantalate, strain, stress, ferroelectric, domain walls, Raman spectroscopy, DFT

I. INTRODUCTION

Lithium niobate (LN) and Lithium tantalate (LT) are cornerstone materials in nonlinear optics and optoelectronics, with established applications ranging from second-harmonic generation [1, 2], over optical ring resonators, to holographic memory devices [3], to name just a few. These devices are based on bulk single crystal platforms and have been constantly optimized over the last decades via meticulous analyses of crystal compositional aspects [4–6], degradation effects [7], defect distribution, and the precise imaging of domain structures [8–10]. Single crystalline LN (or LT) thin films on insulating substrates have recently opened up a completely new scenario. This new platform allows for much higher integrability into existing nanoelectronic and nanophotonic structures [11, 12] and outperforms bulk-based devices due to the submicron-scale confinement of optical modes [13–15].

Nevertheless, the transition towards thin-film LN (TFLN) devices emphasizes the importance of crystal properties that so far have played a minor role in LN bulk investigations and device fabrication. Among these, we count the increased influence of mechanical stress (σ) fields [16, 17], e.g., due to the bonding process of the LN thin film onto the substrate, or occurring as a result of

the poling procedure or waveguide fabrication, which is paramount for the reliable and reproducible production of highly efficient nonlinear optical devices. Accumulated stress does not only increase the chance of critical failure (e.g. due to delamination) [16, 17], but also influences optical key properties such as refractive indices [18, 19] and thus endangers the optical responses of a periodically-poled domain grid [20].

Among established imaging techniques applied for the analysis of LN platforms, Raman spectroscopy can provide critical information about internal mechanical stress. To discriminate the influence of stress fields from other factors, e.g. electrical fields [21] or compositional heterogeneity [22], and to quantify occurring stress markers, it is essential to gain fundamental knowledge on the relation of phonon properties and mechanical stress fields. To date, the only investigations in this regard were conducted via hydrostatic pressure-cells [23, 24]. However, such experiments only investigate the influence of isotropically applied stress. In reality, effects like stress fields in the vicinity of LN DWs, or mechanical stress in LN thin films, are not isotropic [25, 26]. Under these environments, the directionality of stress largely changes the materials properties. Therefore, it is necessary to theoretically predict and experimentally verify the influence of uniaxial stress on phonon properties. This then provides a fundamental reference for future investigations of mechanical stress fields, in analogy to the reference work of Stone *et al.* [21] for incident electrical fields.

In this work, we firstly provide the theoretical prediction on the evolution of the phonon properties in

* email: ekta.singh1@tu-dresden.de

† email: mike.pionteck@theo.physik.uni-giessen.de

LN and LT crystals upon uniaxial compression along all three crystal axes via density functional theory (DFT) in Sec. II A. Secondly, we combine a piezo-driven uniaxial stress cell with a μ -Raman spectroscopy setup to enable the experimental study of stress on the LN crystals. Experimentally, we compare stoichiometric and 5% MgO-doped LN samples compressed along the x,y, and z axes [see Sec. II B]. Sec. III C then provides a discussion of the calculated and measured data.

With this work, we thus provide a basis for the quantitative, local stress analysis in LN and LT platforms via μ -Raman spectroscopy and give a reference for the deeper understanding and further optimization of LN- and LT-based devices.

II. METHODOLOGY

A. Computational Approach

The DFT calculations are performed within the generalized gradient approximation (GGA) [27] in the formulation of Perdew, Burke, and Ernzerhof (PBE) [28] as implemented in the Vienna Ab Initio Simulation Package (VASP) [29]. Thereby, projector augmented wave (PAW) [30] potentials with projectors up to $l = 3$ for Nb and Ta, and $l = 2$ for Li and O have been used, which proved to be accurate enough as demonstrated in a previous work [31]. The electronic wave functions are expanded into a plane-wave basis set up to kinetic energy of 475 eV. In order to model uniaxial stress, the lattice constants of the rhombohedral unit cell were adjusted according to the expression

$$\mathbf{a}_n(\epsilon) = (\mathbf{I} + \epsilon) \mathbf{a}_n(0), \quad (1)$$

where ϵ , \mathbf{I} , $\mathbf{a}_n(0)$, and $\mathbf{a}_n(\epsilon)$ denote the strain tensor, the identity matrix, and the n th unstrained and strained lattice vector, respectively. The strain tensor was then calculated using the elastic compliance tensor S from Ref. [32],

$$\epsilon = S\sigma, \quad (2)$$

and the boundary conditions for uniaxial stress. This means that all components of the stress tensor σ are set to zero, except for the component in the direction of which uniaxial stress is to be exerted. For instance, if uniaxial stress is to be calculated along the x direction, $\sigma_1 \neq 0 = \sigma_2 = \sigma_3 = \sigma_4$ (Voigt notation) is set as boundary condition. Due to constraints of the unit cell sizes, only stoichiometric LN and LT is calculated. However, as later demonstrated by experiments by comparing 5% MgO-doped and stoichiometric LN, it is shown that the results for 5% MgO-doped and stoichiometric LN are comparable, therefore this assumption is justified, to only calculate stoichiometric LN and LT.

The calculations were performed in two ranges for LN and LT: First, the effects of strain, i.e. compressive as well as tensile strain, on the phonon frequencies have been calculated in fine increments up to values reachable in the experiments. Second, calculations for higher values of strains, but more coarse increments, were performed. For LN and LT this procedure has been performed for lower strains up to 0.10%, as well as for higher values up to 2.4%. Here, increments of 0.02% and 0.4% have been chosen, respectively. The Hellmann-Feynman forces are minimized under a threshold value of 0.005 eV/Å by relaxation of the atomic positions. For our calculations of unstrained structures we have used commonly accepted experimental lattice constants ($a_R^{LN} = 5.494$ Å, $\alpha^{LN} = 55.867^\circ$ and $a_R^{LT} = 5.474$ Å, $\alpha^{LT} = 56.171^\circ$) [31].

The Γ -centered phonon frequencies and eigenvectors are derived by the frozen-phonon method [33] without symmetry constraints. For the calculation of the Hessian matrix, atomic displacements of 0.015 Å in each Cartesian direction are considered. Since our approach does not take into account the long-range electric fields accompanying the longitudinal-optical (LO) phonons, our calculations are restricted to transversal-optical (TO) phonons, only. A $8 \times 8 \times 8$ k-point mesh is used to sample the first Brillouin-zone corresponding to the orthorhombic unit cell, which yields 192 irreducible points.

B. Experimental Procedure

In order to complement the above theoretical investigations, we measured the frequency shift of the phonon modes in LN by combining μ -Raman spectroscopy with a uniaxial stress cell [34]. All measurements were performed using a LabRAM HR spectroscope from Horiba in 180° back-scattering geometry. In this setup, a HeNe laser at 632.8 nm wavelength was focused onto the samples using a 100X and 0.9 NA objective. For each data point, two acquisitions were collected for 10 s each, while using a diffraction grating of 1800 grid lines per millimeter for spectral analysis. For these settings, the corresponding spectral resolution is 0.56 cm^{-1} , which was determined as part of the calibration using a He-Ne gas discharge lamp. Here, the plasma line at a wavelength of 671.7 nm has a natural line width of 0.025 nm (0.56 cm^{-1}), which corresponds to the spectral resolution i.e. the standard deviation, which only means how well the two overlapping peaks can be resolved. On the other hand, with the help of the standard error obtained from peak fitting, each peak center can be pinpointed with a 100-1000 times more precision, and this is the quantity we are interested in.

All the samples used in this work were firmly attached to the uniaxial stress cell using black stycast epoxy resin [35] such that the strain is fully transmitted to the sample through the epoxy resin. The force applied to the sample was directly measured through a force sensor attached to the back of the device. This force was later converted to

TABLE I. Description of the samples used for the experimental stress measurement analysis.

sample name	description	size	stress axis
sLN-x	z-cut stoichiometric LN	y × z: 580 × 113 μm ²	x
sLN-y	z-cut stoichiometric LN	x × z: 580 × 113 μm ²	y
5Mg-LN-x	z-cut 5%-MgO doped LN	y × z: 500 × 140 μm ²	x
5Mg-LN-y	z-cut 5%-MgO doped LN	x × z: 400 × 100 μm ²	y
5Mg-LN-z	x-cut 5%-MgO doped LN	y × x: 400 × 100 μm ²	z

stress using the relation

$$\sigma = \frac{F}{A}, \quad (3)$$

where A denotes the cross-section of the samples provided in table I, and F is the force measured by the force sensor. In order to compensate for any charge-induced effects due to the piezoelectric effect, the top and bottom faces of the sample surfaces were electrically grounded using 10 nm-thick chromium electrodes. All the measurements were always performed across the chromium electrodes, which at the given thickness are still sufficiently transparent and do not affect our measurements, as also shown in the past for *in situ* second-harmonic microscopy studies [36].

A total of five samples were measured [see Tab. I]. First, stoichiometric LN, being close to the ideal crystals considered for the theoretical calculations, is measured and used to compare theory with experiment. Second, 5% MgO-doped LN samples are chosen, because they are widely used among the ferroelectrics and integrated optics community due to their low photorefraction and highly conductive domain walls [12, 37–39]. Comparing the results on the stoichiometric and MgO-doped crystals allows us to see whether or not there are any stoichiometry-specific changes in the responses, which would also not be covered by the DFT calculations.

1. Data extraction method

The Raman spectra of single-crystalline LN and LT are well understood and have been investigated thoroughly before [31, 40–43]. The optical phonons of LN and LT consist of four A_1 , five A_2 , and nine doubly-degenerated E phonon branches. Here, A_1 and E are optical branches and are both Raman and Infrared active. In contrast, the A_2 branch is optically inactive. Furthermore, depending on the scattering geometry these branches either appear as TO or LO modes. Conveniently LN and LT peaks are labeled by type of symmetry (A_1 or E), followed by the specific type (TO or LO) and consecutive number counting from low to high frequency. For example, the phonon E(TO₉) labels the ninth, i.e. highest frequency, E-type TO phonon. The assignment of peaks in this work has been performed according to the most recent accepted assignment by Margueron *et al.*, Sanna *et al.* and Rüsing *et al.* [31, 41, 42].

Figure 1(a), (b) and (c) shows example Raman spectra of the 5Mg-LN-x, 5Mg-LN-y, and 5Mg-LN-z samples, respectively. These spectra are measured in different scattering geometries represented by the Porto notation $k_i(e_i, e_s)k_s$, where k_i and k_s represent the direction of incident and scattered light in crystal coordinates, and e_i and e_s denote the direction of polarization of both incoming and Raman scattered beams, respectively [41]. Here, each plot contains 3 spectra, where spectrum A belongs to the unstressed (0 MPa) state of the sample while spectrum B describes a compressed state of the sample. The third is the difference spectrum of the former two. To eliminate the intensity influences in the difference spectrum and to solely highlight the effect of the frequency shift due to applied stress, all the spectra were first normalized individually by subtracting the noise background (if applicable) and divided by the intensity of the highest peak [10]. From the different spectra of Fig. 1(b), it can be clearly noticed that the frequency of the E(TO₁) phonon mode in $\bar{Z}(XY)Z$ geometry increased under compression, while the frequency for $A_1(\text{TO}_1)$ in $\bar{X}(ZZ)X$ geometry decreased. Apart from these large differences, further changes are difficult to notice. So, to quantify frequency shifts as a function of stress, the fitting of the spectra by Lorentzian functions is performed. In this way, the frequencies at the maxima of the phonon peaks were determined for different stress values and plotted against applied stress, such as shown in Fig. 2. Via statistical analysis of the phonon shifts, we are able to deduce the experimental phonon-stress-shift coefficients with a precision of 0.01 cm⁻¹/%.

Additionally, it is well-known [44, 45] that the spectra of congruent or MgO-doped LN show broader and less resolvable peaks as compared to the stoichiometric LN. Here, various peaks overlap with each other, that then leads to a more challenging peak assignment. For example, the pairs E(TO₃)- $A_1(\text{LO}_1)$, $A_1(\text{LO}_2)$ -E(TO₄), and $A_1(\text{LO}_3)$ -E(TO₇) overlap with each other in the $\bar{Z}(XX)Z$ and $\bar{Z}(YY)Z$ geometry of MgO-doped LN. Therefore, in Sec. III A, to avoid any misleading conclusions, for these peaks the Raman shifts with the stress have not been fitted [see Table II and IV].

Furthermore, to find an optimum location on the sample, a series of optimization measurements [see SI for further information] are performed. As a result, all the measurements were performed in the center of the sample and 10 μm below the sample surface.

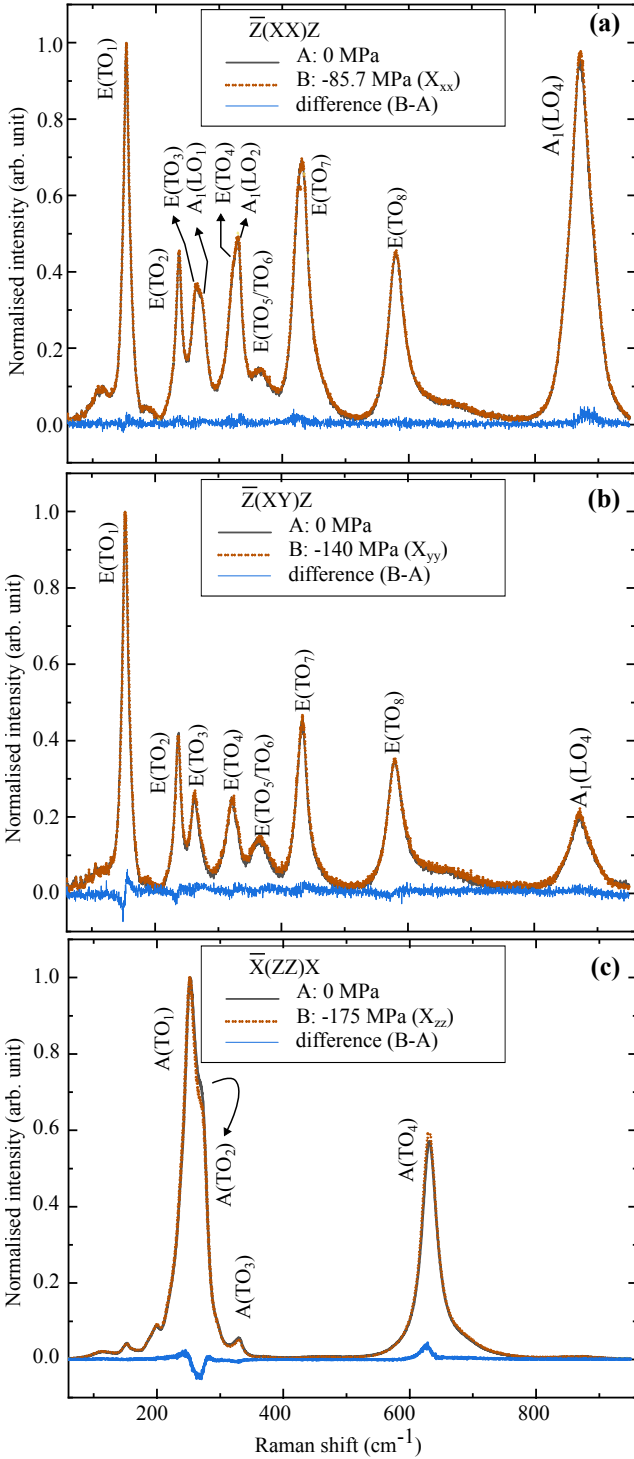


FIG. 1. (a) $\bar{Z}(XX)Z$ Raman spectra of unstressed (0 MPa) and x compressed (-85.7 MPa) 5% MgO-doped LN (5Mg-LN-x). (b) $\bar{Z}(XY)Z$ Raman spectra of unstressed (0 MPa) and y compressed (-140.7 MPa) 5% MgO-doped LN (5Mg-LN-y). (c) $\bar{X}(ZZ)X$ Raman spectra of unstressed (0 MPa) and z compressed (-175 MPa) z-axis of 5% MgO-doped LN (5Mg-LN-z). The difference curve in all (a)-(c) graphs represents the difference spectra between the stressed and unstressed states of the sample.

III. RESULTS

A. Experimental Results

For the sake of simplicity, we only show the pressure dependency for selected phonon modes; the complete results are shown in the Supplement information (SI).

Fig. 2 shows the response of the $E(TO_1)$ phonon mode under x and y compression for both the stoichiometric and 5%-MgO doped LN samples. The three curves in a single plot represent the three different scattering geometries given in Porto's notation. Since the change of the frequency ($\Delta\omega$) with respect to the unstressed state is the quantity of interest, we have plotted the frequencies with respect to the 0 MPa value as a function of stress. Hence, we also account for any offset due to sample mounting or bending effects as discussed in the SI.

The coloured region around the fitted lines show the one-sigma confidence interval, calculated from linear fitting which included the standard error of individual peaks. The $E(TO_1)$ mode shows a linear positive slope for the compression in all cases. In the case of x compression for both sLN-x and 5Mg-LN-x samples, the slope is larger in $\bar{Z}(YY)Z$ measurement geometry. On the other hand, when the same samples are compressed along the y crystallographic axis, the slope is larger for $\bar{Z}(XY)Z$ and $\bar{Z}(XX)Z$ scattering geometries. We have observed this behavior for almost all the phonon modes [see SI]. The value of different slopes in different measurement geometry can be interpreted as the lifting of the two-fold degeneracy of the E-modes predicted by theory as discussed below.

When comparing 5Mg-LN-x/-y and sLN-x/-y, the slopes are similar as shown in Fig. 2. The origin of the small deviations could be due to the presence of defects in doped-LN. This argument is consistent with the work done by Tejerina *et al.*, where they show that doping increases the phonon shift under hydrostatic pressure ($\Delta\omega/\Delta\sigma$) [46], especially for the $A_1(TO_2)$, $A_1(TO_3)$, and $E(TO_4)$ phonon modes. The comparison for other peaks is also summarized in Table II.

As will later be shown by theory, the phonon frequency should decrease under tension with a slightly different magnitude. That is why the phonon response of sample sLN-x is also measured experimentally in $\bar{Z}(YY)Z$ scattering geometry under tension. For tensile strain, the opposite response is observed as expected: the frequency decreased on applying tension to the sample. For example, phonon mode $E(TO_6)$ shows the largest response as for compression with a slope of $-8.15 \pm 2.88 \text{ cm}^{-1}/\text{GPa}$. The plot for $E(TO_6)$ and the slopes for all peaks are provided in SI.

B. Strain Simulation

First, to assess the quality of the models in this work, the calculated phonon frequencies of unstrained stoichio-

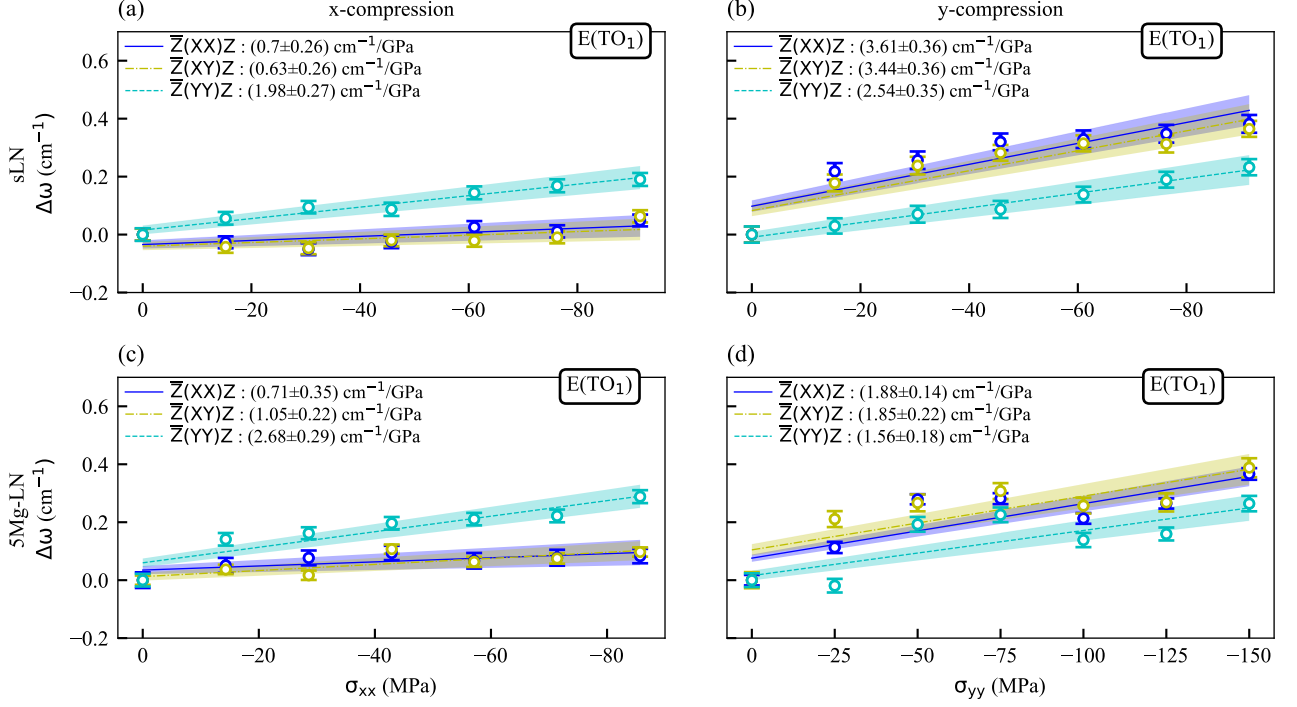


FIG. 2. Measured response of the E(TO_1) phonon mode (a)-(b) in the samples sLN compressed along the x and y axes, respectively and (c)-(d) in the sample 5Mg-LN compressed along the x and the y axes, respectively. The stoichiometric and 5% MgO-doped LN behave similarly.

TABLE II. Experimentally determined Raman shift changes $\Delta\omega$ as a function of stress σ for x compression. The slopes were obtained after linearly fitting the experimental changes in frequency upon x compression. An asterisk labels silent modes [41]. In the case of 5% MgO-doped LN, many peaks overlap with each other [see Fig. 1(a)-(b)], therefore extracting the peak frequency with an acceptable error was not possible. This is represented by the '-' sign.

Phonon modes	sLN-x ($\text{cm}^{-1}/\text{GPa}$)			5Mg-LN-x ($\text{cm}^{-1}/\text{GPa}$)		
	$\bar{Z}(XX)Z$	$\bar{Z}(XY)Z$	$\bar{Z}(YY)Z$	$\bar{Z}(XX)Z$	$\bar{Z}(XY)Z$	$\bar{Z}(YY)Z$
$A_1(LO_1)$	2.13 ± 0.52	*	2.06 ± 0.58	-	*	-
$A_1(LO_2)$	3.29 ± 0.17	*	3.66 ± 0.17	-	*	-
$A_1(LO_3)$	0.39 ± 0.94	*	0.29 ± 0.71	-	*	-
$A_1(LO_4)$	1.96 ± 0.21	*	2.32 ± 0.19	3.07 ± 0.83	*	3.79 ± 0.80
E(TO_1)	0.70 ± 0.26	0.63 ± 0.26	1.98 ± 0.27	0.71 ± 0.35	1.05 ± 0.22	2.68 ± 0.29
E(TO_2)	0.34 ± 0.17	0.26 ± 0.25	1.68 ± 0.16	-0.51 ± 0.45	-0.63 ± 0.52	1.52 ± 0.3
E(TO_3)	1.28 ± 0.44	1.39 ± 0.65	1.67 ± 0.42	-	-	-
E(TO_4)	2.12 ± 0.35	1.56 ± 0.59	3.02 ± 0.4	-	-	-
E($TO_{5/6}$)	6.36 ± 0.98	6.25 ± 1.5	8.17 ± 0.87	5.87 ± 4.23	3.77 ± 3.69	9.38 ± 2.16
E(TO_7)	0.44 ± 0.37	0.86 ± 1.51	1.24 ± 0.22	-	-	-
E(TO_8)	-0.47 ± 0.30	0.37 ± 0.36	3.03 ± 0.27	-0.29 ± 0.8	1.66 ± 0.69	4.32 ± 0.67

metric LN and LT are compared with previous works [31] (all data appear in the SI). Compared to our experiment, the largest deviation from the experimental values for LN and LT occurs for the $A_1(TO_4)$ mode with 20 cm^{-1} and 22 cm^{-1} , respectively. The mean deviation from experimental values for LN and LT is about 8.7 cm^{-1} and 8.4 cm^{-1} . Thus, compared with the mean deviation of the theoretical results of Ref. [31] which was about 10.7 cm^{-1} and 10.8 cm^{-1} for LN and LT, there is

a close agreement with both the theoretical and experimental values. In addition, the typical deviations are also consistent with literature values, such as Refs. [41, 47].

In order to demonstrate the dependence of the phonon frequencies predicted by our calculations, the E(TO_4) mode of LN was chosen [see Fig. 3]. Figures 3(a) and (b) show the results of the calculations with lower and higher strains, respectively. The frequency shift of the E(TO_4) mode has an approximately linear dependence

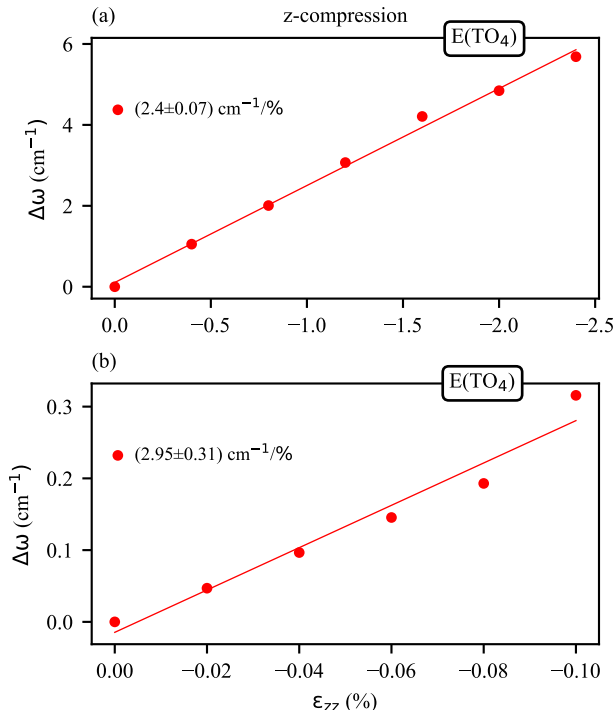


FIG. 3. DFT calculated relative frequency shifts of the E(TO₄) mode of stoichiometric LN as a function of strain in z-direction in (a) steps of 0.4% and (b) steps of 0.02%. The linear fit and the standard deviation of both are plotted and their parameters displayed. The slopes for strain are defined as $(\Delta\omega)/(|\Delta\epsilon|)$ and displayed with the fitting error.

on the applied compression. Such a linear dependence is observed in all of our calculations for each mode for both the compressive and tensile strain in stoichiometric LN and LT. This is consistent with the results of LN and LT under hydrostatic pressure by Mendes-Filho *et al.* [23]. In Fig. 3(a) the frequency increases up to 6 cm⁻¹ and in (b) up to 0.3 cm⁻¹.

Our calculations predict for stoichiometric LN and LT that the degeneracy of the E modes is lifted under strain applied along the x and y direction due to the reduction of the threefold symmetry. This results in splitting into two branches, which is consistent with previous studies on various 2D materials, that reported a mode splitting under strain due to the reduction of symmetry [48, 49]. Consequently, for strains applied along the x and y direction, all E modes are considered separately. For example, the E(TO₉) mode for compression in x and y directions has a significant splitting [see Fig. 4(a)]. In contrast, it is noticeable that the E(TO₉) mode remains degenerate for z compression since the considered strains in the z direction of both LN and LT do not lead to any reduced symmetry. This is the case for all E modes of LN and LT under strain.

Since the slopes, for strains in the x and y directions of LN and LT, are very similar [see SI] due to the sym-

TABLE III. Calculated slopes of transversal A₁ and E modes of stoichiometric LN under compressive and tensile strain, and stoichiometric LT under compressive strain in the x-direction at higher strains in cm⁻¹/%. The slopes for strain are defined as $(\Delta\omega)/(|\Delta\epsilon|)$.

Phonon mode	LN comp. $\Delta\omega$ [cm ⁻¹ /%]	LN tens. $\Delta\omega$ [cm ⁻¹ /%]	LT comp. $\Delta\omega$ [cm ⁻¹ /%]
A ₁ (TO ₁)	1.31	-2.87	3.16
A ₁ (TO ₂)	3.64	-4.78	4.51
A ₁ (TO ₃)	5.18	-7.08	4.84
A ₁ (TO ₄)	3.95	-3.79	3.93
E(TO ₁)	0.68/3.26	-1.56/-3.37	1.32/1.45
E(TO ₂)	1.52/0.32	-3.69/0.04	2.68/0.91
E(TO ₃)	1.09/2.24	-4.40/-1.56	2.62/2.45
E(TO ₄)	2.19/1.98	-3.42/-1.65	2.73/2.40
E(TO ₅)	6.58/6.09	-9.57/-13.57	7.39/8.31
E(TO ₆)	12.84/12.39	-4.93/-3.76	14.82/13.58
E(TO ₇)	4.18/2.72	1.01/-1.52	0.83/2.02
E(TO ₈)	3.63/0.91	-0.67/-4.51	4.65/1.54
E(TO ₉)	1.36/4.94	0.70/-5.12	4.00/3.45

metry of the crystals, Table III shows only the slopes for strain in the x direction. With the exception of the A₁(TO₁) and A₁(TO₄) modes, compressive strain leads to an increase in frequency, while tensile strain leads to a decrease in frequencies, which is consistent with results from previous research on other materials [50, 51]. Comparing the slopes under the compressive and tensile strain of LN, we find that they hardly differ for the individual modes. This behavior is not surprising, however, it is not universal, as shown for a 2D material by Pak *et al.* [50]. Although under both compressive and tensile strain the E(TO_{5/6}) modes have the largest frequency shifts, the E(TO₆) mode has a larger slope than the E(TO₅) mode under compression. However, this relation turns around under tensile strain as can be seen in Table III. This applies to strain in the x and y direction for both LN and LT (see SI).

In addition, the results of LT under compression are listed in Table III for the same modes. In direct comparison with the results of LN, they are very similar along both directions, as well as magnitude. This is in agreement with Mendes-Filho *et al.* [23] and expected since LN and LT are isostructural. Nevertheless, there are some small deviations. In particular, the degeneracy lifting is attenuated compared to LN. For instance, the upper branch of the E(TO₁) mode has a notable lower slope than that of LN. Also, the E(TO₉) mode exhibits a significantly attenuated degeneracy lift for LT under compression than for LN. These deviations can be explained with the help of the eigenvectors. In Fig. 5 the eigenvectors of A₁(TO₁₋₄) and E(TO₁₋₉) are shown in the rhombohedral unit cell [31, 41]. Such modes with high vibrational contributions from Nb and Ta ions, like the E(TO₁) mode, lead to a slightly different vibrational behavior [31]. The modes that have in turn low contributions of Nb and Ta ions with respect to their eigenvectors,

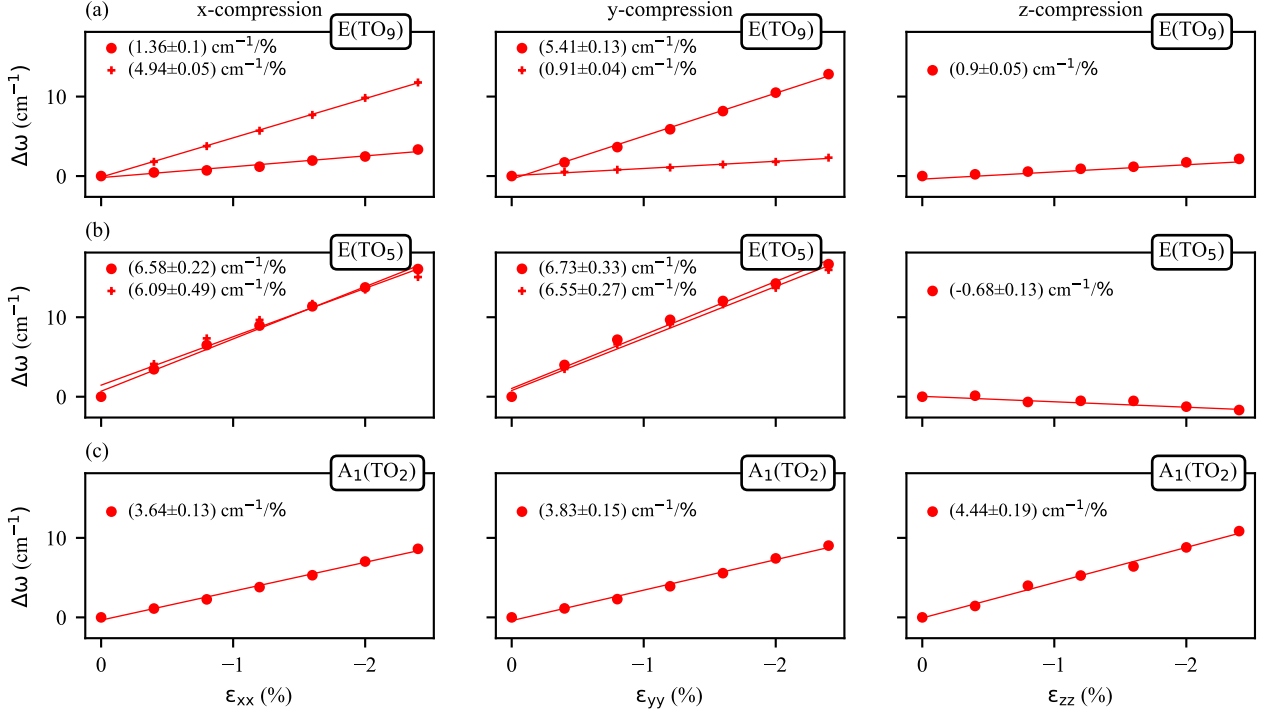


FIG. 4. The DFT calculated relative frequency shifts of (a) E(TO₉) (first row), (b) E(TO₅) (second row) and (c) A₁(TO₂) (third row) modes of stoichiometric LN as a function of strain in steps of 0.4% along the x, y and z direction. The slopes for strain are defined as $(\Delta\omega)/(|\Delta\epsilon|)$ and displayed with the fitting error.

are very similar under compression of LN and LT. Since in the E(TO₉) mode, the displacement of O is more involved than that of Nb/Ta, the reason for the difference between LN and LT may be due to the nature of Nb/Ta-O bond, similar to observations in Refs. [31, 41]. The mean Nb-O distance (2.02 Å) is larger than that of Ta-O (2.00 Å). Stronger bonding with the oxygen atoms, and thus larger deformation of the oxygen octahedron, might be the reason for the difference between LN and LT concerning the E(TO₉) mode. Also, slight differences in E(TO₇) and E(TO₈), which are pure distortions of the oxygen octahedron, might be related to the different Nb/Ta-O bonds.

The E(TO_{5/6}) and A₁(TO₂) modes are characteristic for LN and LT under strain, since these have particularly high slopes, as shown in Table III and Fig. 4(b) and (c). This is also in agreement with Ref. [23]. The E(TO_{5/6}) are especially sensitive to strain in the x and y directions. This can be explained by a simple analysis of their eigenvectors. In Fig. 5 it can be seen that these two modes, in contrast to all other modes, are characterized by particularly large displacements of the lithium ions parallel to the x-y-plane. Hence, these modes are most affected when the distances between the ions parallel to the x-y-plane are shortened. The A₁(TO₂) mode has among the largest slope for strain along the z direction. This can be reasonably explained in terms of the eigenvectors as well. As seen in Fig. 5, the ions of the A₁(TO₂) mode

vibrate in z direction. When compression in the z direction shortens the bond length between the ions parallel to their displacement, the frequency is expected to increase. As the eigenvectors of the A₁(TO₂) mode point most in the z direction, it consequently has the largest slope compared to all other modes when compressed in the z-direction. All further data and results on LN and LT under compressive and tensile strain are provided in the SI.

C. Discussion: Comparing theory and experiment

As mentioned in the introduction section, the calculations are performed in units of strain and the experiments are performed in units of stress. In order to compare both results we have converted the experimental values of stress into values of strain using the equation given below:

$$\sigma = E\epsilon, \quad (4)$$

where E is Young's Modulus of a sample [52]. The calculated value of Young's Moduli of LN along the x, y, and z axes are 173.6 GPa, 173.07 GPa, and 201.0 GPa, respectively [see calculations in SI]. For every measured stress, we calculated the respective strain value and plotted the corresponding frequency shift along with the theoretical data as a function of strain [see Fig. 6]. Since the

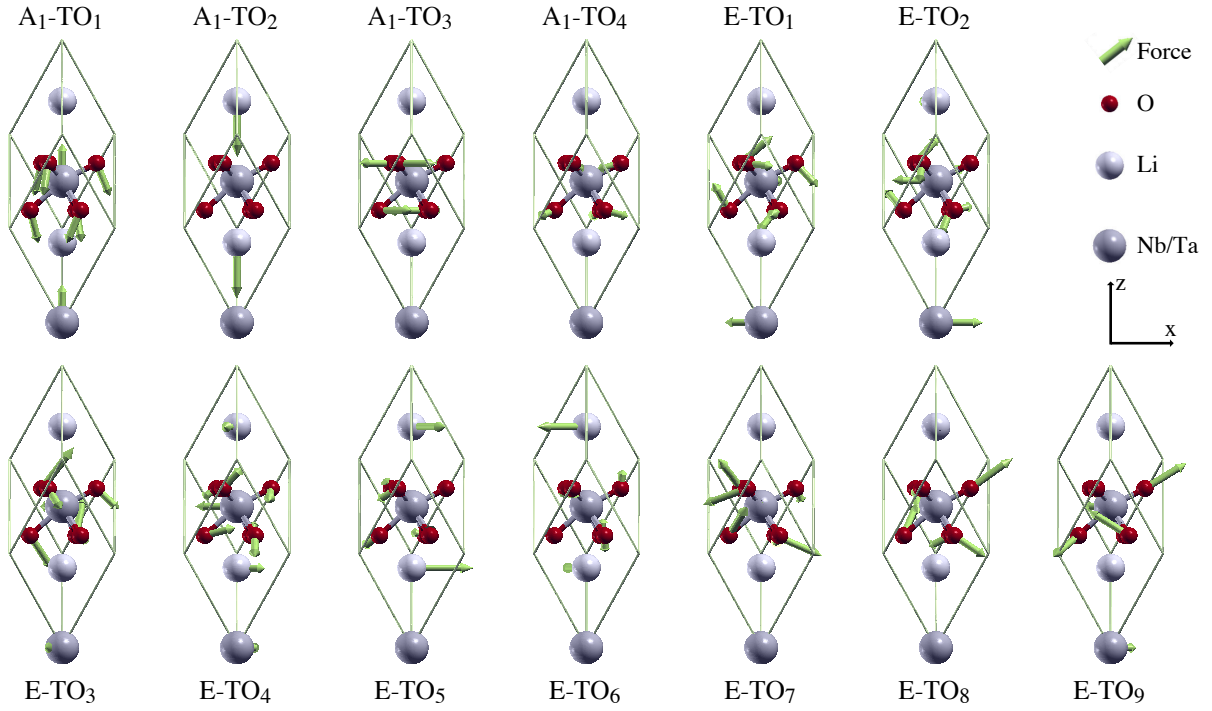


FIG. 5. The eigenvectors of the Raman active vibrations of unstrained stoichiometric LN and LT in the rhombohedral unit cell of the transversal phonon modes with A_1 and E symmetry. Thereby light grey is denoted as Li, dark grey as Nb/Ta, and red as O ion, while the green arrows represent the displacement direction.

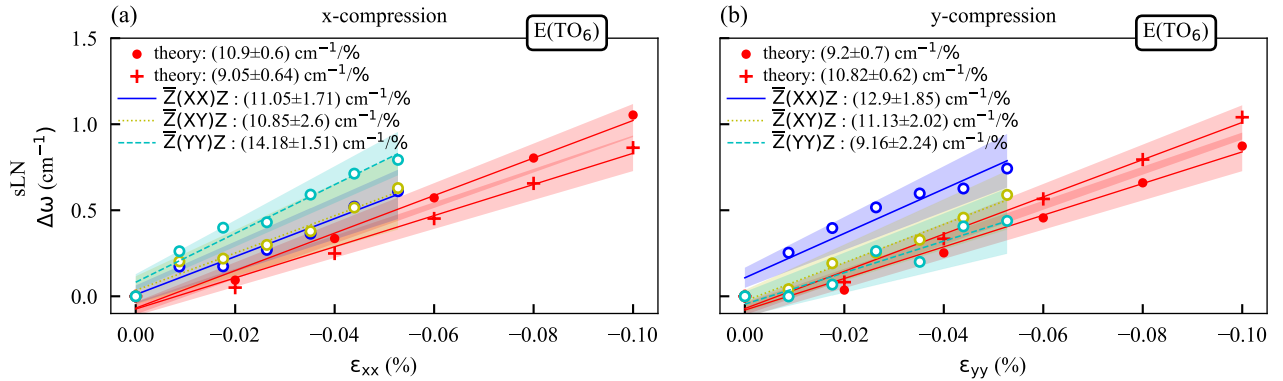


FIG. 6. Comparison of the experimental and theoretical frequency shift (at lower strains): (a)-(b) $E(TO_6)$ phonon mode under compression along the x and y axes of stoichiometric LN. The shaded region around all the curves is the confidence interval of the linear fit.

stoichiometric samples are the closest system to the stoichiometric system considered for theoretical calculations, they are compared with theoretical data in Fig. 6.

For x compression, theoretically, the $E(TO_6)$ mode shows lifting of the degeneracy in accordance with the results of Sec. III B. For a more accurate comparison, the slopes for higher strains for y and z compression are listed in Table IV. The theoretical results on the degeneracy lifting offer a new interpretation of the experimental results. In particular, comparing the data for the $E(TO_7)$ mode with compression in the x direction, it can be seen

that the data for the $\bar{Z}(YY)Z$ resembles the upper branch, and its slope of the theoretical data, and the data for the $\bar{Z}(XY)Z$ and $\bar{Z}(XX)Z$ geometry is similar to the theoretical data and slope of the lower branch. For y compression, the same can be observed, with the $\bar{Z}(XY)Z$ and $\bar{Z}(XX)Z$ geometries having the higher slope, respectively, and the $\bar{Z}(YY)Z$ having the lower slope, i.e. the slopes flip for y compression. Consequently, it can be assumed that with the help of different scattering geometries the lifting of the degeneracy by x and y compression can be reproduced experimentally.

Based on this interpretation, it can be concluded that the experimental and theoretical data fit very well. For a more accurate comparison, the slopes for higher strains for y and z compression are listed in Table IV.

Interpreting the experimental data as lifting the degenerate E modes on x and y compression can also help characterize compressed LN. From the data, it can be implied that one has x compressed LN when the $\bar{Z}(YY)Z$ geometry measures a higher slope than for the $\bar{Z}(XY)Z$ and $\bar{Z}(XX)Z$ geometries. If, on the other hand, one has y compressed LN, this argument just reverts. In contrast, if no splitting E modes are observed in different scattering geometries, it can be concluded that the LN under investigation must be a z-compressed sample. Furthermore, the experimental comparison in Fig. 6 and Table IV, confirms the prediction that the $E(TO_6)$ mode is the mode with highest slope for x and y compression. In comparison with Sec. III A and III B, the slopes for x compression are very similar to those for y compression.

As concluded from the experimental results in Sec. III A, the 5% MgO-doped LN responds equally well as the stoichiometric LN, upon compression. We compare the 5Mg-LN-z sample with theoretical data of stoichiometric LN for z compression. As theoretically predicted and confirmed by the experiment, both $E(TO_7)$ and $A_1(TO_4)$ modes show a linear dependence on z compression [see Fig.7(a)-(b)]. For the $E(TO_7)$ mode, no degeneracy lifting occurs for z compression, which can also be seen in the experimental data. This investigation provides another rule for characterizing compressed LN.

As described in Sec. III B the frequencies of most modes are linearly increasing with increasing compression. For a few modes, this is not the case, e.g., for the $A_1(TO_4)$ modes. For this mode, a linear decrease in frequency with increasing compression is theoretically predicted. This is consistent with experimental measurements, as shown in Fig. 7(b). This unusual behavior can also be explained with the help of the eigenvectors. In Fig. 5 it can be seen that the oxygen ions move towards the positively charged niobium ions and then away from them. If z compression reduces the distance between the cations, then as the oxygen ions displace away from niobium, the restoring force towards niobium may be weakened by the shortened distance to the lithium ions, which also exert the Coulomb force on the negatively-charged oxygen ions. Thus, the frequency for z compression might be reduced. In a similar way, this explanation can also be applied to $A_1(TO_1)$ modes. All other modes for comparison for z compression are shown in Table IV.

IV. CONCLUSIONS

Experimental and theoretical phonon frequencies as a function of uniaxial strain have been evaluated and compared for LN and LT. This investigation has shown that all phonon modes are affected by strain. Both theoretical and experimental results are consistent with the roughly

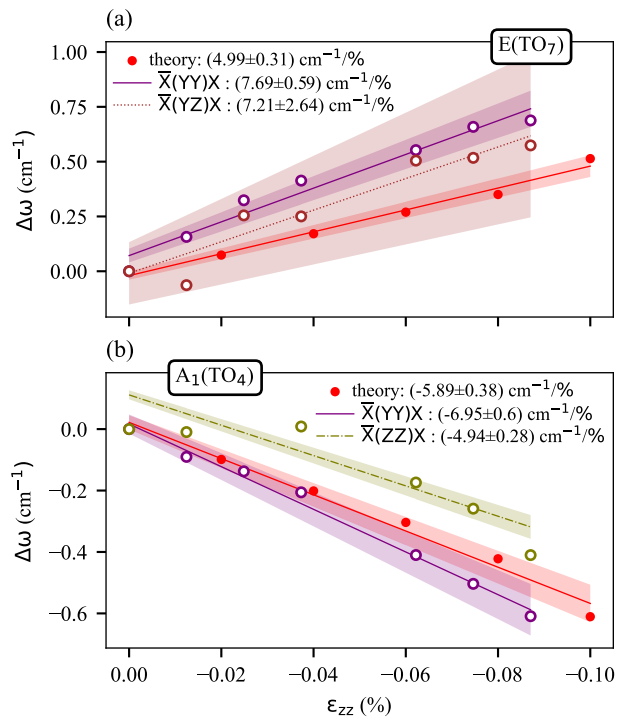


FIG. 7. Comparison of theoretical stoichiometric and experimental 5Mg-LN-z sample when compressing along the z-direction, for frequency shifts of (a) $E(TO_7)$ and (b) $A_1(TO_4)$. $E(TO_7)$ shows a positive slope while $A_1(TO_4)$ shows a negative slope for z compression.

linear behavior of the modes and can be reasonably explained by an analysis of the calculated eigenvectors. The linearity of the slopes confirms the previous works under hydrostatic pressure and under external electric fields [21, 23].

Accordingly, the obtained slopes provide reference values for the peak shifts. Furthermore, with the help of the slopes, it is possible to characterize compressed LN crystals and, hence, the vicinity of domain walls and wave guides in LN. Our experimental and theoretical investigations show that x and y compressed LN has particularly high peak shifts for the $E(TO_{5/6})$ modes and z compressed LN for the $A_1(TO_2)$, $E(TO_7)$ and $E(TO_8)$ modes [23].

Furthermore, calculations have shown that the degeneracy of the E modes is lifted for x and y compression upon symmetry reduction. The splitting has also been observed in our experiments when measured under different scattering geometries. Based on our theoretical and experimental investigations three rules can be formulated to characterize the direction of uniaxial compression of a LN sample using different scattering geometries. This only concerns the E modes. The sample is x compressed if higher frequency shifts are observed for the $\bar{Z}(YY)Z$ geometry than for the $\bar{Z}(XY)Z$ and $\bar{Z}(XX)Z$ geometries when applying the same compressive stress. For y com-

TABLE IV. Comparison between the theoretical response at higher strains with the experimental response of the samples sLN-y and 5Mg-LN-z. Asterisks label modes that are Raman silent in the given scattering geometry.

Modes	sLN-y (cm ⁻¹ /%)				5Mg-LN-z (cm ⁻¹ /%)			
	$\bar{Z}(XX)Z$	$\bar{Z}(XY)Z$	$\bar{Z}(YY)Z$	Theory	$\bar{X}(ZZ)X$	$\bar{X}(YZ)X$	$\bar{X}(YY)X$	Theory
A ₁ (LO ₁)	8.01 ± 1.41	*	6.31 ± 0.68	*	*	*	*	*
A ₁ (LO ₂)	7.95 ± 0.35	*	6.18 ± 0.68	*	*	*	*	*
A ₁ (LO ₃)	4.24 ± 1.94	*	2.82 ± 0.68	*	*	*	*	*
A ₁ (LO ₄)	6.75 ± 0.33	*	5.12 ± 0.68	*	*	*	*	*
A ₁ (TO ₁)	*	*	*	1.15	-4.97 ± 0.93	*	-5.10 ± 5.63	-2.97
A ₁ (TO ₂)	*	*	*	3.83	7.49 ± 1.08	*	5.98 ± 4.73	4.44
A ₁ (TO ₃)	*	*	*	4.47	4.54 ± 1.24	*	-0.19 ± 1.4	0.65
A ₁ (TO ₄)	*	*	*	3.87	-4.94 ± 0.65	*	-6.94 ± 0.60	-4.91
E(TO ₁)	6.27 ± 0.63	5.97 ± 0.63	4.41 ± 0.60	3.25/0.83	*	0.40 ± 0.44	-0.15 ± 0.54	-0.61
E(TO ₂)	5.48 ± 0.35	4.84 ± 0.35	1.56 ± 0.34	-0.70/2.36	*	0.61 ± 0.53	1.08 ± 1.51	-2.55
E(TO ₃)	7.56 ± 1.04	5.81 ± 1.04	4.68 ± 1.07	1.34/2.21	*	1.46 ± 1.75	1.44 ± 7.44	0.50
E(TO ₄)	4.5 ± 0.69	4.44 ± 0.69	2.42 ± 0.68	2.03/2.12	*	5.43 ± 0.92	-3.84 ± 11.74	2.40
E(TO ₅)	*	*	*	6.73/6.55	*	*	*	-0.68
E(TO ₆)	12.9 ± 1.85	11.13 ± 1.85	9.16 ± 2.02	13.00/11.86	*	0.72 ± 2.31	1.90 ± 1.9	-0.94
E(TO ₇)	3.41 ± 0.68	1.64 ± 0.68	1.23 ± 0.82	4.12/2.01	*	7.21 ± 2.64	7.69 ± 0.59	4.75
E(TO ₈)	8.56 ± 0.48	6.72 ± 0.48	3.27 ± 0.70	3.75/1.00	*	6.73 ± 0.62	6.20 ± 5.94	3.35
E(TO ₉)	-	-	-	5.41/0.91	-	-	-7.95 ± 13.41	0.90

pression, the opposite is the case. In contrast, when no differences are observed between the frequency shift of the E modes for various scattering geometries, it can be concluded that the sample under investigation must be z compressed.

Furthermore, the calculation has shown that the behavior of LT under strain is not significantly different from that of LN. Experimentally, it has additionally revealed that the frequency shifts under compression of stoichiometric and 5% MgO-doped LN are comparable. As DWs in LN and LT can be represented in the first approximation as strained lattices, our investigation might be helpful to understand the Raman signal of DWs. Further studies of strained samples, concerning e.g., their linear and non-linear optical response might further help to characterize ferroelectric DWs.

ACKNOWLEDGMENTS

We thank Dr Clifford W. Hicks for the help in designing the stress cell used in the measurements. The authors gratefully acknowledge the financial support by the Deutsche Forschungsgemeinschaft (DFG) through joint DFG-ANR project TOPELEC (No. EN-434/41-1 and No. ANR-18-CE92-0052), FOR5044 (ID: 426703838; <http://www.For5044.de>), as well as the Würzburg-Dresden Cluster of Excellence "ct.qmat" (EXC 2147). Calculations for this research were conducted on the Lichtenberg high-performance computer of the TU Darmstadt and at the Höchstleistungsrechenzentrum Stuttgart (HLRS). The authors furthermore acknowledge the computational resources provided by the HPC Core Facility and the HRZ of the Justus-Liebig-Universität Gießen. Furthermore, we thank D. Bieberstein and T. Gemming from IFW Dresden for assistance with dicing of the wafers and support from the International Max Planck Research School for Chemistry and Physics of Quantum Materials.

- [1] G. D. Miller, R. G. Batchko, W. M. Tulloch, D. R. Weise, M. M. Fejer, and R. L. Byer, "42%-efficient single-pass cw second-harmonic generation in periodically poled lithium niobate," *Optics Letters*, vol. 22, p. 1834, dec 1997.
- [2] R. Mouras, M. D. Fontana, P. Bourson, and A. V. Postnikov, "Lattice site of Mg ion in LiNbO₃ crystal determined by Raman spectroscopy," *Journal of Physics: Condensed Matter*, vol. 12, pp. 5053–5059, jun 2000.
- [3] A. Yariv, S. S. Orlov, and G. A. Rakuljic, "Holographic storage dynamics in lithium niobate: theory and experiment," *Journal of the Optical Society of America B*, vol. 13, p. 2513, nov 1996.
- [4] N. Iyi, K. Kitamura, F. Izumi, J. Yamamoto, T. Hayashi, H. Asano, and S. Kimura, "Comparative study of defect structures in lithium niobate with different compositions," *Journal of Solid State Chemistry*, vol. 101, pp. 340–352, dec 1992.
- [5] A. Bartasyte, S. Margueron, T. Baron, S. Oliveri, and P. Boulet, "Toward High-Quality Epitaxial LiNbO₃ and LiTaO₃ Thin Films for Acoustic and Optical Applica-

- tions,” *Advanced Materials Interfaces*, vol. 4, no. 8, 2017.
- [6] Y. Li, W. G. Schmidt, and S. Sanna, “Defect complexes in congruent LiNbO₃ and their optical signatures,” *Physical Review B*, vol. 91, p. 174106, may 2015.
 - [7] Y. Furukawa, K. Kitamura, S. Takekawa, A. Miyamoto, M. Terao, and N. Suda, “Photorefraction in LiNbO₃ as a function of [Li]/[Nb] and MgO concentrations,” *Applied Physics Letters*, vol. 77, pp. 2494–2496, oct 2000.
 - [8] G. Stone and V. Dierolf, “Influence of ferroelectric domain walls on the Raman scattering process in lithium tantalate and niobate,” *Optics Letters*, vol. 37, p. 1032, mar 2012.
 - [9] G. F. Nataf, M. Guennou, A. Haußmann, N. Barrett, and J. Kreisel, “Evolution of defect signatures at ferroelectric domain walls in Mg-doped LiNbO_{2.3},” *physica status solidi (RRL) - Rapid Research Letters*, vol. 10, pp. 222–226, mar 2016.
 - [10] M. Rüsing, S. Neufeld, J. Brockmeier, C. Eigner, P. Mackwitz, K. Spychala, C. Silberhorn, W. G. Schmidt, G. Berth, A. Zrenner, and S. Sanna, “Imaging of 180° ferroelectric domain walls in uniaxial ferroelectrics by confocal Raman spectroscopy: Unraveling the contrast mechanism,” *Physical Review Materials*, vol. 2, p. 103801, oct 2018.
 - [11] X. Wang, P. O. Weigel, J. Zhao, M. Ruesing, and S. Mookherjea, “Achieving beyond-100-GHz large-signal modulation bandwidth in hybrid silicon photonics Mach Zehnder modulators using thin film lithium niobate,” *APL Photonics*, vol. 4, p. 096101, sep 2019.
 - [12] M. Rusing, P. O. Weigel, J. Zhao, and S. Mookherjea, “Toward 3D Integrated Photonics Including Lithium Niobate Thin Films: A Bridge Between Electronics, Radio Frequency, and Optical Technology,” *IEEE Nanotechnology Magazine*, vol. 13, pp. 18–33, aug 2019.
 - [13] D. Zhu, L. Shao, M. Yu, R. Cheng, B. Desiatov, C. J. Xin, Y. Hu, J. Holzgrafe, S. Ghosh, A. Shams-Ansari, E. Puma, N. Sinclair, C. Reimer, M. Zhang, and M. Lončar, “Integrated photonics on thin-film lithium niobate,” *Advances in Optics and Photonics*, vol. 13, p. 242, jun 2021.
 - [14] M. G. Vazimali and S. Fathpour, “Applications of thin-film lithium niobate in nonlinear integrated photonics,” *Advanced Photonics*, vol. 4, pp. 1–18, may 2022.
 - [15] C. Wang, M. Zhang, B. Stern, M. Lipson, and M. Lončar, “Nanophotonic lithium niobate electro-optic modulators,” *Optics Express*, vol. 26, p. 1547, jan 2018.
 - [16] R. Takigawa, T. Tomimatsu, E. Higurashi, and T. Asano, “Residual Stress in Lithium Niobate Film Layer of LNOI/Si Hybrid Wafer Fabricated Using Low-Temperature Bonding Method,” *Micromachines*, vol. 10, p. 136, feb 2019.
 - [17] K. Prabhakar, R. J. Patton, and R. M. Reano, “Stress reduction and wafer bow accommodation for the fabrication of thin film lithium niobate on oxidized silicon,” *Journal of Vacuum Science & Technology B*, vol. 39, p. 062208, dec 2021.
 - [18] M. Friedrich, W. G. Schmidt, A. Schindlmayr, and S. Sanna, “Optical properties of titanium-doped lithium niobate from time-dependent density-functional theory,” *Physical Review Materials*, vol. 1, p. 034401, aug 2017.
 - [19] G. Zisis, C. Y. J. Ying, P. Ganguly, C. L. Sones, E. Söergel, R. W. Eason, and S. Mailis, “Enhanced electro-optic response in domain-engineered LiNbO₃ channel waveguides,” *Applied Physics Letters*, vol. 109, p. 021101, jul 2016.
 - [20] S. Reitzig, M. Rüsing, J. Zhao, B. Kirbus, S. Mookherjea, and L. M. Eng, ““Seeing Is Believing”—In-Depth Analysis by Co-Imaging of Periodically-Poled X-Cut Lithium Niobate Thin Films,” *Crystals*, vol. 11, p. 288, mar 2021.
 - [21] G. Stone, B. Knorr, V. Gopalan, and V. Dierolf, “Frequency shift of Raman modes due to an applied electric field and domain inversion in LiNbO₃,” *Physical Review B*, vol. 84, p. 134303, oct 2011.
 - [22] M. D. Fontana and P. Bourson, “Microstructure and defects probed by Raman spectroscopy in lithium niobate crystals and devices,” *Applied Physics Reviews*, vol. 2, p. 040602, dec 2015.
 - [23] J. Mendes-Filho, V. Lemos, and F. Cerdelra, “Pressure dependence of the Raman spectra of LiNbO₃ and LiTaO₃,” *Journal of Raman Spectroscopy*, vol. 15, p. 367–369, dec 1984.
 - [24] A. M. Heyns and J. B. Clark, “Effect of pressure on the Raman spectra of solids: 1-KC103,” *Journal of Raman Spectroscopy*, vol. 14, pp. 342–346, oct 1983.
 - [25] T. Jach, S. Kim, V. Gopalan, S. Durbin, and D. Bright, “Long-range strains and the effects of applied field at 180° ferroelectric domain walls in lithium niobate,” *Physical Review B*, vol. 69, p. 064113, feb 2004.
 - [26] D. A. Scrymgeour, V. Gopalan, A. Itagi, A. Saxena, and P. J. Swart, “Phenomenological theory of a single domain wall in uniaxial trigonal ferroelectrics: Lithium niobate and lithium tantalate,” *Physical Review B*, vol. 71, p. 184110, may 2005.
 - [27] J. P. Perdew, J. A. Chevary, S. H. Vosko, K. A. Jackson, M. R. Pederson, D. J. Singh, and C. Fiolhais, “Erratum: Atoms, molecules, solids, and surfaces: Applications of the generalized gradient approximation for exchange and correlation,” *Physical Review B*, vol. 48, pp. 4978–4978, aug 1993.
 - [28] J. P. Perdew, K. Burke, and M. Ernzerhof, “Generalized Gradient Approximation Made Simple,” *Physical Review Letters*, vol. 77, pp. 3865–3868, oct 1996.
 - [29] G. Kresse and J. Furthmüller, “Efficient iterative schemes for ab initio total-energy calculations using a plane-wave basis set,” *Physical Review B*, vol. 54, pp. 11169–11186, oct 1996.
 - [30] P. E. Blöchl, “Projector augmented-wave method,” *Physical Review B*, vol. 50, pp. 17953–17979, dec 1994.
 - [31] S. Sanna, S. Neufeld, M. Rüsing, G. Berth, A. Zrenner, and W. G. Schmidt, “Raman scattering efficiency in LiTaO₃ and LiNbO₃ crystals,” *Physical Review B*, vol. 91, p. 224302, jun 2015.
 - [32] A. W. Warner, M. Onoe, and G. A. Coquin, “Determination of Elastic and Piezoelectric Constants for Crystals in Class (3 m),” *The Journal of the Acoustical Society of America*, vol. 42, pp. 1223–1231, dec 1967.
 - [33] W. G. Schmidt, F. Bechstedt, and G. P. Srivastava, “III-V(110) surface dynamics from an ab initio frozen-phonon approach,” *Physical Review B*, vol. 52, pp. 2001–2007, jul 1995.
 - [34] E. Singh, H. Beccard, Z. H. Amber, J. Ratzenberger, C. W. Hicks, M. Rüsing, and L. M. Eng, “Tuning domain wall conductivity in bulk lithium niobate by uniaxial stress,” *Phys. Rev. B*, vol. 106, p. 144103, Oct 2022.
 - [35] Henkel Loctite®, “Loctite stycast 2850ft,” 2014.
 - [36] B. Kirbus, C. Godau, L. Wehmeier, H. Beccard, E. Beyreuther, A. Haußmann, and L. M. Eng, “Real-Time 3D Imaging of Nanoscale Ferroelectric Domain

- Wall Dynamics in Lithium Niobate Single Crystals under Electric Stimuli: Implications for Domain-Wall-Based Nanoelectronic Devices,” *ACS Applied Nano Materials*, vol. 2, pp. 5787–5794, sep 2019.
- [37] C. Godau, T. Kämpfe, A. Thiessen, L. M. Eng, and A. Haußmann, “Enhancing the Domain Wall Conductivity in Lithium Niobate Single Crystals,” *ACS Nano*, vol. 11, pp. 4816–4824, may 2017.
- [38] P. S. Bednyakov, B. I. Sturman, T. Sluka, A. K. Tagantsev, and P. V. Yudin, “Physics and applications of charged domain walls,” *npj Computational Materials*, vol. 4, p. 65, dec 2018.
- [39] C. S. Werner, S. J. Herr, K. Buse, B. Sturman, E. Söergel, C. Razzaghi, and I. Breunig, “Large and accessible conductivity of charged domain walls in lithium niobate,” *Scientific Reports*, vol. 7, p. 9862, dec 2017.
- [40] A. Bartaszyte, S. Margueron, A. M. Glazer, E. Simon, I. Gregora, S. Huband, and P. A. Thomas, “Vibrational modes and overlap matrix of $\text{LiNb}_{1-x}\text{Ta}_x\text{O}_3$ mixed crystals,” *Physical Review B*, vol. 99, p. 094306, mar 2019.
- [41] M. Rüsing, S. Sanna, S. Neufeld, G. Berth, W. G. Schmidt, A. Zrenner, H. Yu, Y. Wang, and H. Zhang, “Vibrational properties of $\text{LiNbO}_{1-x}\text{Ta}_x\text{O}_3$ mixed crystals,” *Physical Review B*, vol. 93, p. 184305, may 2016.
- [42] S. Margueron, A. Bartaszyte, A. M. Glazer, E. Simon, J. Hlinka, I. Gregora, and J. Gleize, “Resolved E-symmetry zone-centre phonons in LiTaO_3 and LiNbO_3 ,” *Journal of Applied Physics*, vol. 111, p. 104105, may 2012.
- [43] A. Irzhak, D. Irzhak, V. Khvostikov, K. Pundikov, D. Roshchupkin, and R. Fahrtdinov, “Effect of local changes in the composition of the $\text{LiNb}_{1-x}\text{Ta}_x\text{O}_3$ single crystal on the Raman spectra,” *Journal of Raman Spectroscopy*, vol. 53, pp. 969–976, may 2022.
- [44] N. V. Sidorov and M. N. Palatnikov, “Raman spectra of lithium niobate crystals heavily doped with zinc and magnesium,” *Optics and Spectroscopy*, vol. 121, pp. 842–850, dec 2016.
- [45] A. Ridah, P. Bourson, M. D. Fontana, and G. Malovichko, “The composition dependence of the Raman spectrum and new assignment of the phonons in LiNbO_3 ,” *Journal of Physics: Condensed Matter*, vol. 9, pp. 9687–9693, nov 1997.
- [46] M. Tejerina, K. Pereira da Silva, A. Goñi, and G. Torchia, “Hydrostatic-pressure dependence of raman-active optical phonons in nd:mg:linbo_3 ,” *Optical Materials*, vol. 36, no. 2, pp. 581–583, 2013.
- [47] P. Hermet, M. Veithen, and P. Ghosez, “First-principles calculations of the nonlinear optical susceptibilities and Raman scattering spectra of lithium niobate,” *Journal of Physics: Condensed Matter*, vol. 19, p. 456202, nov 2007.
- [48] D. Doratotaj, J. R. Simpson, and J.-A. Yan, “Probing the uniaxial strains in MoS_2 using polarized Raman spectroscopy: A first-principles study,” *Physical Review B*, vol. 93, p. 075401, feb 2016.
- [49] M. Huang, H. Yan, C. Chen, D. Song, T. F. Heinz, and J. Hone, “Phonon softening and crystallographic orientation of strained graphene studied by Raman spectroscopy,” *Proceedings of the National Academy of Sciences of the United States of America*, vol. 106, no. 18, pp. 7304–7308, 2009.
- [50] S. Pak, J. Lee, Y.-W. Lee, A.-R. Jang, S. Ahn, K. Y. Ma, Y. Cho, J. Hong, S. Lee, H. Y. Jeong, H. Im, H. S. Shin, S. M. Morris, S. Cha, J. I. Sohn, and J. M. Kim, “Strain-Mediated Interlayer Coupling Effects on the Excitonic Behaviors in an Epitaxially Grown MoS_2/WS_2 van der Waals Heterobilayer,” *Nano Letters*, vol. 17, pp. 5634–5640, sep 2017.
- [51] B. G. Oliveira, A. Zabardasti, H. Goudarziafshar, and M. Salehnassaj, “The electronic mechanism ruling the dihydrogen bonds and halogen bonds in weakly bound systems of $\text{H}_3\text{SiH}-\dots\text{HOX}$ and $\text{H}_3\text{SiH}-\dots\text{XOH}$ ($X = \text{F}, \text{Cl}, \text{and Br}$),” *Journal of Molecular Modeling*, vol. 21, p. 77, apr 2015.
- [52] R. E. Newnham, *Properties of Materials*. Oxford University Press, nov 2004.

* The authors contributed equally to this paper.

Supplemental Information: Phonon shifts of lithium niobate under uniaxial stress

Ekta Singh^{*,1,*} Mike N. Pionteck^{*,2,†} Sven Reitzig,¹ Michael
Lange,¹ Michael Rüsing,¹ Lukas M. Eng,^{1,3} and Simone Sanna²

¹*Institut für Angewandte Physik, Technische Universität Dresden, 01062 Dresden, Germany*

²*Institut für Theoretische Physik, Justus-Liebig-Universität Gießen, Gießen, Germany*

³*ct.qmat: Dresden-Würzburg Cluster of Excellence—EXC 2147,
TU Dresden, 01062 Dresden, Germany*

(Dated: October 25, 2022)

S1. OPTIMIZING THE MEASUREMENTS

In the stress cell, the samples are mounted onto two sample plates above a 1 mm gap. This gap is the region where the maximum strain is expected. The strain is gradually transmitted through the epoxy to the sample. Therefore, finding an optimum location on the samples is central for this work to achieve reproducible results.

In order to do so, we performed a series of optimization measurements. With the help of Raman spectroscopy the distribution of the strain was measured along the length of the sample (i.e. the strained axes), see Fig. S1(a). Here, a stoichiometric LN (sLN-x) sample was compressed to the stress of -91.5 MPa along the crystallographic x-axis. To see the gradual increase of the strain towards the center from both ends of the sample, the Raman spectra were measured at 200 points over a 4 mm length of the sample with increments of $20\ \mu\text{m}$. As the $E(\text{TO}_6)$ phonon is one of the isolated peaks and also as demonstrated in the main text, this phonon shows the strongest response to the stress, we now show the peak frequency of the $E(\text{TO}_6)$ as a function of position. Indeed, the plot shows that the frequency of $E(\text{TO}_6)$ mode increases towards the center of the compressed sLN-x and stays constant over ≈ 1 mm length, indicating that the strain is transmitted to the sample through the epoxy and is uniform in the center of the sample. Based on this result we decided to measure always in the center of the 1 mm gap of the device, which is easily identified in the optical microscope. One may also notice the two red colored arrows pointing to missing or shifted data points. This was observed in all the phonon modes. These likely indicate dust particles sitting on the sample surface. Such areas were avoided during subsequent measurements.

Furthermore, since the sample is sitting on top of the 1 mm gap, in order to investigate a bending effect, depth scans on the same compressed sample at -91.5 MPa stress (sLN-x) were performed, and the results were compared to a reference unstressed stoichiometric LN sample, as shown in Fig. S1(b). To achieve the depth scan, the laser was focused at different depths along the sample thickness. The first thing to notice is that the frequency of phonon mode $E(\text{TO}_6)$ decreases with a slightly different slope when moving into the depth of both the unstressed and stressed samples. The error bars in the unstressed sample are of the same order of magnitude as the slope, indicating no strain inhomogeneity with depth for the unstressed sample. On the other hand for the sample sLN-x compressed at -91.5 MPa,

* email: ekta.singh1@tu-dresden.de

† email: mike.pionteck@theo.physik.uni-giessen.de

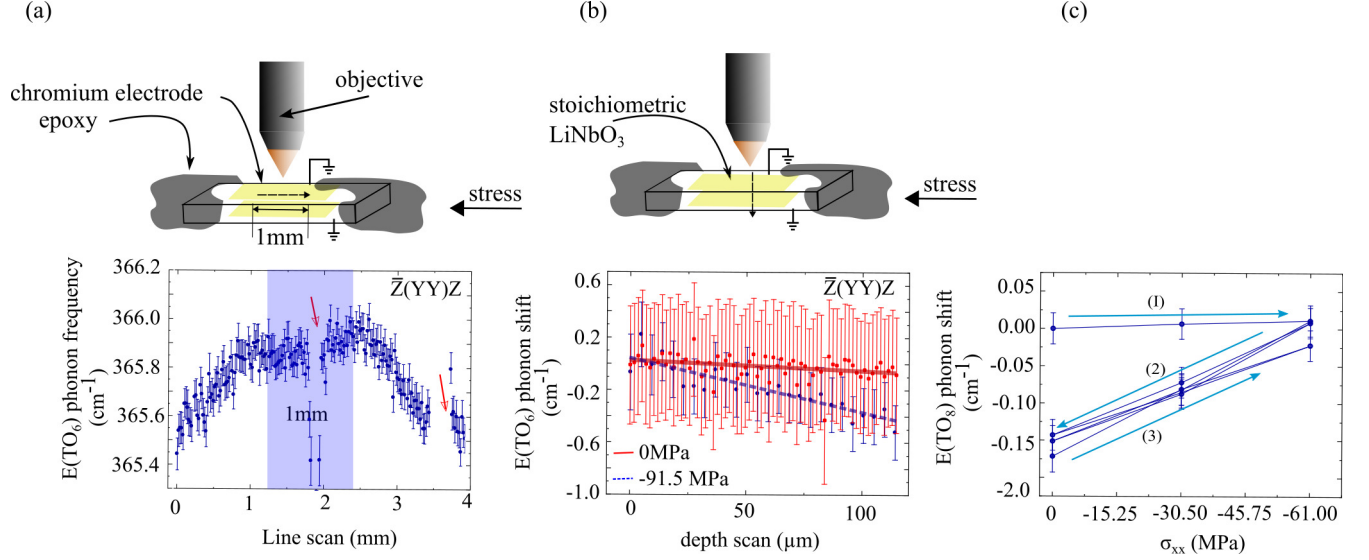


FIG. S1. Optimization of the measurement on sample sLN-x. (a) Line scan at -91.5 MPa. (b) depth scan on unstressed and compressed sLN-x based on the response of the $E(\text{TO}_6)$ phonon frequency. (c) Hysteresis behavior of the $E(\text{TO}_8)$ phonon mode with applied stress (σ_{xx}) applied along the crystallographic x-axis during the first and following cycles. Here, after one initial cycle, a reproducible behavior was established.

we observe a small but significant slope of $(-3.87 \pm 0.411) \times 10^{-3} \text{cm}^{-1} \mu\text{m}^{-1}$, which can be interpreted in terms of the sample is bent downwards. Such slight bends may be caused by very small inhomogeneities in the mounting, variations in thickness, or width of the sample, and cannot be avoided completely.

As each sample is mounted individually, it may bend slightly upwards or downwards, which will cause a slight offset error in the frequency, as additional uniaxial stress is added or subtracted. Assuming the determined depth dependency for this sample is an average slope for up- or downward bends, we can use this to estimate the error that is caused by this effect. Whenever a sample is bent, this will result in three distinct regions in the sample:

- At a line parallel to the horizontal center no bending strain will be experienced (neutral line).
- The region above will experience compressive (tensile) strain for a downward (upward) bending.
- In the region below the neutral line the behavior will be reversed.

Our measurements were always performed at a depth of approximately $10\ \mu\text{m}$ with respect to the top surface, as this region could be located easily. All the samples in this work had thicknesses in the range of $100\ \mu\text{m}$. Therefore, our measured spot was conservatively estimated at about a $50\ \mu\text{m}$ distance from the neutral line. Therefore, if the sample is bent up- or downwards, an additional frequency shift at each phonon is added. For example, for the $E(\text{TO}_6)$ based on the depth dependency determined in the paragraph above this amounts to an offset of $0.19 \pm 0.021\ \text{cm}^{-1}$ at a stress of $91.5\ \text{MPa}$. If we now compare this value to the error in the peak frequency due to fitting, which for the $E(\text{TO}_6)$ in the sample sLN-x, for example, is $\Delta\omega = 0.08\ \text{cm}^{-1}$ then this is approximate twice the error for the largest stresses. Please note, that this error will proportionally decrease for smaller applied forces, as the bending will proportionally decrease as well. However, compared to the stress response of the $E(\text{TO}_6)$ [see Table II in the main paper] this error is still small. For other phonons, a similar relative error will be observed, as both the bending error and the stress-dependent shift are proportional.

In addition to the strain inhomogeneity along the length and depth of the sample, we expect that the hardening of the epoxy (during curing) may put the sample under stress even before measurement, which may relax during measurement cycles. Indeed, we observed that some phonon modes such as $E(\text{TO}_8)$ showed a hysteresis behavior. As seen from Fig. S1(c), the first cycle shows hysteresis but typically after 3 cycles, the response was reproducible within error limits. As mentioned earlier this behavior is a result of epoxy and indirectly sample relaxation after the first cycle. Therefore, such a procedure was performed for each sample.

In conclusion, these are three optimization steps that were always considered before starting any measurement on a new sample.

S2. YOUNG'S MODULUS CALCULATION FOR LITHIUM NIOBATE

Mechanical properties of a solid are described by the fourth rank elastic stiffness tensor c_{ijkl} and the elastic compliance tensor s_{ijkl} . s_{ijkl} is the inverse of elastic stiffness tensor (c_{ijkl}), i.e. $s_{ijkl} = c_{ijkl}^{-1}$. Both these tensors connect the symmetric and second rank strain (ϵ_{ij}) and stress (σ_{ij}) tensors to each other. The stress is defined by force applied to a unit area of material, while the strain is the relative change of length in a material. The SI unit of the stress is given by Nm^{-2} , while a strain is a unitless quantity. In the elastic regime, c_{ijkl} and s_{ijkl} are connected to stress and the strain via Hooke's law:

$$\begin{aligned}\epsilon_{ij} &= s_{ijkl}\sigma_{kl} \\ \sigma_{ij} &= c_{ijkl}\epsilon_{kl}\end{aligned}\tag{S1}$$

Equation (S1) is written in a tensorial form, which can be simplified into matrix form by using Voigt notation, where indices $i, j, k,$ and l can take values from 1, 2, and 3 which correspond to x, y, and z directions, respectively.

$$\begin{array}{lll}11 \rightarrow 1 & 12 \rightarrow 6 & 13 \rightarrow 5 \\ 22 \rightarrow 2 & 21 \rightarrow 6 & 23 \rightarrow 4 \\ 33 \rightarrow 3 & 31 \rightarrow 5 & 32 \rightarrow 4\end{array}$$

Since, the strain and the stress tensors are symmetric ($ij = ji$), the 81 components (3^4) of the fourth rank stiffness and compliance tensor are reduced to 36 independent components, where $c_{ijkl} = c_{jikl} = c_{jilk} = c_{ijlk}$. It is due to this fact that the elastic constants can be written in 6×6 matrix. This matrix can be further simplified to 21 independent components because the stiffness coefficients are second-order derivatives of the mechanical energy density with respect to strain components. The order in which the differentiation is taken does not affect the energy density, which makes the stiffness coefficients symmetric as well.

Furthermore, the symmetries of a crystal can simplify these matrices even more with the help of Neumann's law [1]. In the case of ferroelectric LiNbO_3 crystal, which belongs to the trigonal crystal system and $3m$ point group, the final form of the matrices is given as follows [1, 2].

Elastic stiffness matrix of LiNbO_3

$$\begin{bmatrix} c_{11} & c_{12} & c_{13} & c_{14} & 0 & 0 \\ c_{12} & c_{22} & c_{13} & -c_{14} & 0 & 0 \\ c_{13} & c_{13} & c_{33} & 0 & 0 & 0 \\ c_{14} & -c_{14} & 0 & c_{44} & 0 & 0 \\ 0 & 0 & 0 & 0 & c_{44} & c_{14} \\ 0 & 0 & 0 & 0 & c_{14} & \frac{1}{2}(c_{11} - c_{12}) \end{bmatrix}$$

Elastic compliance matrix of LiNbO₃

$$\begin{bmatrix} s_{11} & s_{12} & s_{13} & s_{14} & 0 & 0 \\ s_{12} & s_{22} & s_{13} & -s_{14} & 0 & 0 \\ s_{13} & s_{13} & s_{33} & 0 & 0 & 0 \\ s_{14} & -s_{14} & 0 & s_{44} & 0 & 0 \\ 0 & 0 & 0 & 0 & s_{44} & 2s_{14} \\ 0 & 0 & 0 & 0 & 2s_{14} & 2(s_{11} - s_{12}) \end{bmatrix}$$

TABLE S1. The room temperature value of elastic compliance and stiffness coefficients at the constant electric field for LiNbO₃.

Compliance coefficients ($\times 10^{-11} \text{ m}^2\text{N}^{-1}$)	s_{11}	s_{12}	s_{13}	s_{14}	s_{33}	s_{44}
[3]	0.578	-0.101	-0.147	-0.102	0.502	0.170
Stiffness coefficients ($\times 10^{11} \text{ Nm}^{-2}$)	c_{11}	c_{12}	c_{13}	c_{14}	c_{33}	c_{44}
[3]	2.03	0.53	0.75	0.09	2.45	0.60

The values of these coefficients are measured by Warner et.al., provided in table S1. However, the stoichiometry of LiNbO₃ is not provided by them in that paper [3]. Assuming that the values of c_{ijkl} coefficients do not change dramatically for the 5% MgO-doped and stoichiometric LiNbO₃, the values given in table S1 have been used in this thesis for further calculations of the Young's Modulus. Using the matrix form of equation (S1), the stress and the strain can be written as equation (S2) and (S3) as follows:

$$\begin{aligned} \epsilon_1 &= s_{11}\sigma_1 + s_{12}\sigma_2 + s_{13}\sigma_3 + s_{14}\sigma_4 \\ \epsilon_2 &= s_{12}\sigma_1 + s_{22}\sigma_2 + s_{13}\sigma_3 - s_{14}\sigma_4 \\ \epsilon_3 &= s_{13}\sigma_1 + s_{13}\sigma_2 + s_{33}\sigma_3 \\ \epsilon_4 &= s_{14}\sigma_1 - s_{14}\sigma_2 + s_{44}\sigma_4 \end{aligned} \tag{S2}$$

and

$$\begin{aligned}
\sigma_1 &= c_{11}\epsilon_1 + c_{12}\epsilon_2 + c_{13}\epsilon_3 + c_{14}\epsilon_4 \\
\sigma_2 &= c_{12}\epsilon_1 + c_{22}\epsilon_2 + c_{13}\epsilon_3 - c_{14}\epsilon_4 \\
\sigma_3 &= c_{13}\epsilon_1 + c_{13}\epsilon_2 + c_{33}\epsilon_3 \\
\sigma_4 &= c_{14}\epsilon_1 - c_{14}\epsilon_2 + c_{44}\epsilon_4
\end{aligned}
\tag{S3}$$

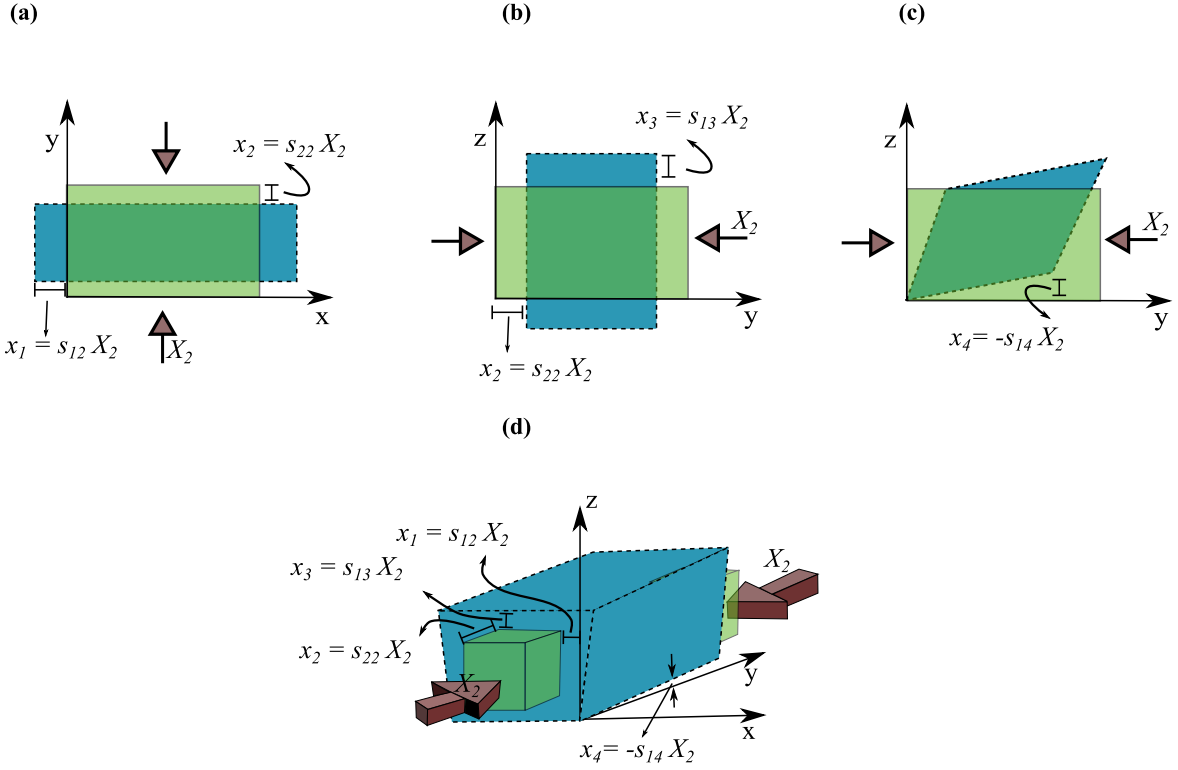


FIG. S2. Distribution of the strain according to equation S2, when the compressive stress is applied only along y-axis in LiNbO_3 ($\sigma_1 = 0, \sigma_2 \neq 0, \sigma_3 = 0$). Green color represents unstrained and blue color represents the strained shape of the rectangular shape crystal according to the equations (S2) : (a) Normal strain ϵ_1 and ϵ_2 alone. (b) Normal strain ϵ_3 alone. (c) Shear strain ϵ_4 alone. (d) All the strains from (a), (b), and (c) are combined together in a 3-dimensional image.

In order to get the Young's Modulus along x-axis, we need the ratio $E_{11} = \frac{\sigma_1}{\epsilon_1}$, which can be obtained by dividing σ_1 in equation (S3) by ϵ_1 , as follows.

$$E_{11} = \frac{\sigma_1}{\epsilon_1} = c_{11} + c_{12} \frac{\epsilon_2}{\epsilon_1} + c_{13} \frac{\epsilon_3}{\epsilon_1} + c_{14} \frac{\epsilon_4}{\epsilon_1}
\tag{S4}$$

where $\frac{\epsilon_2}{\epsilon_1}$, $\frac{\epsilon_3}{\epsilon_1}$ or $\frac{\epsilon_4}{\epsilon_1}$ are quantities equal to the negative of Poisson's ratio. These ratios can also be obtained by using equation (S2). For uniaxial stress along the x-axis, all the stress components except σ_1 should be zero. Using this information one can calculate the Poisson's ratio of LiNbO₃ as follows:

$$\begin{aligned}\nu_{12} &= -\frac{\epsilon_2}{\epsilon_1} = -\left(\frac{s_{12}}{s_{11}}\right) = -\left(\frac{-1.01}{5.78}\right) = 0.1747 \\ \nu_{13} &= -\frac{\epsilon_3}{\epsilon_1} = -\left(\frac{s_{13}}{s_{11}}\right) = -\left(\frac{-1.47}{5.78}\right) = 0.254 \\ \nu_{14} &= -\frac{\epsilon_4}{\epsilon_1} = -\left(\frac{s_{14}}{s_{11}}\right) = -\left(\frac{-1.02}{5.78}\right) = 0.17647\end{aligned}\tag{S5}$$

Inserting these values in equation (S4) one can calculate Young's Modulus along the x-axis. The same method of calculation is applied to calculate the Young's Modulus of LiNbO₃ along the y and z axes, for values see table S2.

TABLE S2. Calculated Young's Modulus of LiNbO₃ along the x, y, and z crystallographic axes

E_{11} (GPa)	E_{22} (GPa)	E_{33} (GPa)
173.6	173.07	201.0

S3. RESULTS

A. Experiment

In this section all the experimental slopes of compressed samples sln-x/y, 5Mg-LN-x/y/z are provided in the tables S3, S5, and S6 respectively. Table S4 provides experimental slopes of the tensile stress on sample sLN-x only.

TABLE S3. Experimental phonon frequency shift values $\Delta\omega$ of stoichiometric lithium niobate upon uniaxial compression along the x- and y-axis.

Phonon modes	sLN-x ($\text{cm}^{-1}/\text{GPa}$)			sln-y ($\text{cm}^{-1}/\text{GPa}$)		
	$\bar{Z}(\text{XX})\text{Z}$	$\bar{Z}(\text{XY})\text{Z}$	$\bar{Z}(\text{YY})\text{Z}$	$\bar{Z}(\text{XX})\text{Z}$	$\bar{Z}(\text{XY})\text{Z}$	$\bar{Z}(\text{YY})\text{Z}$
A ₁ (LO ₁)	2.13 ± 0.52	*	2.06 ± 0.58	4.61 ± 0.81	*	3.64 ± 1.89
A ₁ (LO ₂)	3.29 ± 0.17	*	3.66 ± 0.17	4.58 ± 0.20	*	3.56 ± 0.60
A ₁ (LO ₃)	0.39 ± 0.94	*	0.29 ± 0.71	2.44 ± 1.11	*	$1.62 \pm$
A ₁ (LO ₄)	1.96 ± 0.21	*	2.32 ± 0.19	3.89 ± 0.19	*	2.95 ± 0.39
E(TO ₁)	0.7 ± 0.26	0.63 ± 0.26	1.98 ± 0.27	3.62 ± 0.36	3.44 ± 0.36	2.54 ± 0.35
E(TO ₂)	0.34 ± 0.17	0.26 ± 0.25	1.68 ± 0.16	3.16 ± 0.20	2.79 ± 0.20	0.9 ± 0.20
E(TO ₃)	1.28 ± 0.44	1.39 ± 0.65	1.67 ± 0.42	4.35 ± 0.6	3.35 ± 0.6	2.7 ± 0.62
E(TO ₄)	2.12 ± 0.35	1.56 ± 0.59	3.02 ± 0.4	2.59 ± 0.4	2.56 ± 0.4	1.39 ± 0.39
E(TO _{5/6})	6.36 ± 0.98	6.25 ± 1.5	8.17 ± 0.87	7.43 ± 1.06	6.41 ± 1.06	5.28 ± 1.16
E(TO ₇)	0.44 ± 0.37	0.86 ± 1.51	1.24 ± 0.22	1.97 ± 0.39	0.94 ± 0.39	0.71 ± 0.47
E(TO ₈)	-0.47 ± 0.3	0.37 ± 0.36	3.03 ± 0.27	4.93 ± 0.27	3.87 ± 0.27	1.89 ± 0.41

TABLE S4. Experimental phonon frequency shift values $\Delta\omega$ of stoichiometric lithium niobate upon uniaxial tension along the x-axis.

Tension sLN-x ($\text{cm}^{-1}/\text{GPa}$), $\bar{Z}(YY)Z$						
$A_1(\text{LO}_1)$	$A_1(\text{LO}_2)$	$A_1(\text{LO}_3)$	$A_1(\text{LO}_4)$	$E(\text{TO}_1)$	$E(\text{TO}_2)$	$E(\text{TO}_3)$
-3.92 ± 2.39	-2.35 ± 0.57	0.35 ± 2.6	-1.2 ± 0.55	-4.04 ± 0.93	-2.01 ± 0.6	-3.01 ± 1.72
$E(\text{TO}_4)$	$E(\text{TO}_{5/6})$	$E(\text{TO}_7)$	$E(\text{TO}_8)$			
-2.7 ± 1.35	-8.15 ± 2.88	-0.86 ± 0.81	-6.01 ± 0.85			

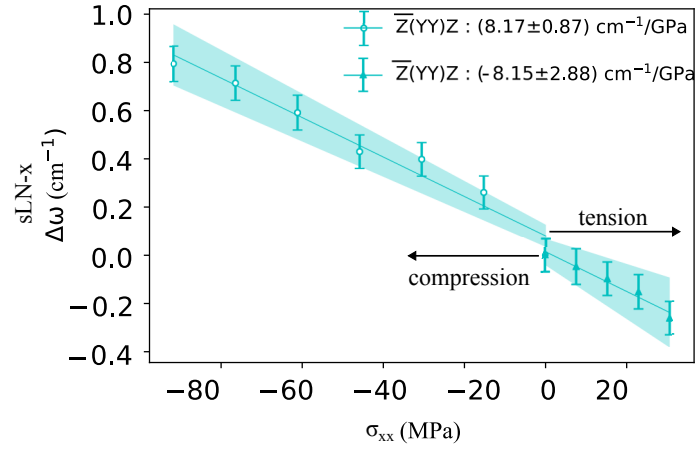


FIG. S3. $E(\text{TO}_6)$ phonon response under compression and tension along the x-axis in $\bar{Z}(YY)Z$ scattering geometry.

TABLE S5. Experimental phonon frequency shift values $\Delta\omega$ of 5% MgO-doped lithium niobate upon uniaxial stress along the x- and y-axis. In the case of 5% MgO-doped LN, many peaks overlap with each other, therefore extracting the peak frequency with an acceptable error was not possible. This is represented by '-' sign.

Phonon modes	5Mg-LN-x ($\text{cm}^{-1}/\text{GPa}$)			5Mg-LN-y ($\text{cm}^{-1}/\text{GPa}$)		
	$\bar{Z}(\text{XX})Z$	$\bar{Z}(\text{XY})Z$	$\bar{Z}(\text{YY})Z$	$\bar{Z}(\text{XX})Z$	$\bar{Z}(\text{XY})Z$	$\bar{Z}(\text{YY})Z$
A ₁ (LO ₁)	-	*	-	-	*	-
A ₁ (LO ₂)	-	*	-	-	*	-
A ₁ (LO ₃)	-	*	-	-	*	-
A ₁ (LO ₄)	3.07 ± 0.83	*	3.79 ± 0.8	2.49 ± 0.42	*	2.09 ± 0.45
E(TO ₁)	0.71 ± 0.35	1.05 ± 0.22	2.68 ± 0.29	1.88 ± 0.14	1.85 ± 0.22	1.56 ± 0.18
E(TO ₂)	-0.51 ± 0.45	-0.63 ± 0.52	1.52 ± 0.3	1.64 ± 0.22	0.77 ± 0.33	0.83 ± 0.3
E(TO ₃)	-	-	-	-	-	-
E(TO ₄)	-	-	-	-	-	-
E(TO _{5/6})	0.71 ± 0.35	1.05 ± 0.22	2.68 ± 0.29	1.88 ± 0.14	1.85 ± 0.22	1.56 ± 0.18
E(TO ₇)	-	-	-	-	-	-
E(TO ₈)	-0.29 ± 0.8	1.66 ± 0.69	4.32 ± 0.67	2.46 ± 0.39	2.23 ± 0.59	1.06 ± 0.48

TABLE S6. Experimental phonon frequency shift values $\Delta\omega$ of 5% MgO-doped lithium niobate upon uniaxial compression along the z-axis.

Phonon modes	5Mg-LN-z ($\text{cm}^{-1}/\text{GPa}$)		
	$\bar{X}(\text{ZZ})\text{X}$	$\bar{X}(\text{YZ})\text{X}$	$\bar{X}(\text{YY})\text{X}$
A ₁ (TO ₁)	-2.47 ± 0.63	*	-2.53 ± 2.8
A ₁ (TO ₂)	3.72 ± 0.70	*	2.97 ± 2.17
A ₁ (TO ₃)	2.23 ± 4.44	*	-0.09 ± 0.70
A ₁ (TO ₄)	-2.46 ± 0.14	*	-3.46 ± 0.30
E(TO ₁)	*	0.2 ± 0.22	-0.07 ± 0.27
E(TO ₂)	*	0.3 ± 0.26	0.54 ± 0.75
E(TO ₃)	*	0.72 ± 0.87	0.07 ± 0.37
E(TO ₄)	*	2.7 ± 0.46	-1.91 ± 5.84
E(TO _{5/6})	*	0.36 ± 1.15	0.94 ± 3.19
E(TO ₇)	*	3.58 ± 1.31	3.83 ± 0.3
E(TO ₈)	*	3.38 ± 0.31	3.08 ± 2.95

B. Theory

In order to compare the calculated phonon frequencies in unstrained LN and LT with Ref. [4], they are displayed in Table S7 and S8. In addition, Table S9 and S10 show all the slopes of LN and LT under uniaxial compressive and tensile strain.

TABLE S7. Calculated frequencies of the Raman active phonon modes in unstrained LN in comparison with calculated and measured frequencies of Ref. [4].

Phonon mode	Theory [cm^{-1}]	Theory [cm^{-1}] [4]	Exp. [cm^{-1}] [4]
A ₁ (TO ₁)	242	239	252–255
A ₁ (TO ₂)	282	289	275–276
A ₁ (TO ₃)	350	353	333–334
A ₁ (TO ₄)	613	610	633
E(TO ₁)	150	148	150–151
E(TO ₂)	216	216	237
E(TO ₃)	265	262	262–263
E(TO ₄)	319	323	320–321
E(TO ₅)	372	380	367–369
E(TO ₆)	384	391	367–369
E(TO ₇)	420	423	432
E(TO ₈)	577	579	580–581
E(TO ₉)	668	667	664

TABLE S8. Calculated frequencies of the Raman active phonon modes in unstrained LT in comparison with calculated and measured frequencies of Ref. [4].

Phonon mode	Theory [cm^{-1}]	Theory [cm^{-1}] [4]	Exp. [cm^{-1}] [4]
A ₁ (TO ₁)	200	209	209–210
A ₁ (TO ₂)	255	286	256–257
A ₁ (TO ₃)	369	376	359–360
A ₁ (TO ₄)	578	591	600
E(TO ₁)	139	144	143
E(TO ₂)	193	199	210
E(TO ₃)	247	253	254–257
E(TO ₄)	313	319	315–317
E(TO ₅)	370	409	383–384
E(TO ₆)	384	420	383–384
E(TO ₇)	452	459	460–465
E(TO ₈)	579	590	592
E(TO ₉)	658	669	661–662

TABLE S9. Calculated slopes of transversal A_1 and E modes of LN under compressive and tensile strain in the x, y and z direction for strains in steps of 0.2% in $\text{cm}^{-1}/\%$. The slopes for strain are defined as $(\Delta\omega)/(|\Delta\epsilon|)$.

Phonon modes	compressive strain ($\text{cm}^{-1}/\%$)			tensile strain ($\text{cm}^{-1}/\%$)		
	x direction	y direction	z direction	x direction	y direction	z direction
$A_1(\text{TO}_1)$	1.31	1.15	-2.97	-2.87	-2.76	2.59
$A_1(\text{TO}_2)$	3.64	3.83	4.44	-4.78	-5.04	-5.20
$A_1(\text{TO}_3)$	5.18	4.47	0.65	-7.08	-5.76	-0.32
$A_1(\text{TO}_4)$	3.95	3.87	-4.91	-3.79	-3.61	5.36
$E(\text{TO}_1)$	0.68/3.26	3.25/0.83	-0.61	-1.56/-3.37	-3.58/-1.57	0.30
$E(\text{TO}_2)$	1.52/0.32	-0.70/2.36	-2.55	-3.69/-0.04	-1.19/-1.51	1.14
$E(\text{TO}_3)$	1.09/2.24	1.34/2.21	0.50	-4.40/-1.56	-2.99/-3.06	-0.53
$E(\text{TO}_4)$	2.19/1.98	2.03/2.12	2.40	-3.42/-1.65	-1.55/-3.29	-2.56
$E(\text{TO}_5)$	6.58/6.09	6.73/6.55	-0.68	-9.57/-13.57	-13.97/-11.17	1.29
$E(\text{TO}_6)$	12.84/12.39	13.00/11.86	-0.94	-4.93/-3.76	-2.57/-5.68	1.12
$E(\text{TO}_7)$	4.18/2.72	4.12/2.01	4.75	1.01/-1.52	0.98/-1.43	-4.08
$E(\text{TO}_8)$	3.63/0.91	3.75/1.00	3.35	-0.67/-4.51	-1.17/-4.33	-2.57
$E(\text{TO}_9)$	1.36/4.94	5.41/0.91	0.90	0.70/-5.12	-4.67/0.19	-0.52

TABLE S10. Calculated slopes of transversal A_1 and E modes of LT under compressive and tensile strain in the x, y and z direction for strains in steps of 0.4% in $\text{cm}^{-1}/\%$. The slopes for strain are defined as $(\Delta\omega)/(|\Delta\epsilon|)$.

Phonon modes	compressive strain ($\text{cm}^{-1}/\%$)			tensile strain ($\text{cm}^{-1}/\%$)		
	x direction	y direction	z direction	x direction	y direction	z direction
$A_1(\text{TO}_1)$	3.16	3.11	-2.78	-2.40	-2.41	2.58
$A_1(\text{TO}_2)$	4.51	4.43	3.77	-3.66	-3.50	-3.93
$A_1(\text{TO}_3)$	4.84	3.87	1.71	1.51	-6.90	-1.60
$A_1(\text{TO}_4)$	3.98	1.92	-4.93	-4.64	-4.28	4.93
$E(\text{TO}_1)$	1.32/1.45	1.82/0.98	-0.49	-0.55/-2.28	-1.87/-1.03	0.45
$E(\text{TO}_2)$	2.68/0.91	0.22/3.45	-3.36	-3.96/-0.59	-1.84/-2.91	2.00
$E(\text{TO}_3)$	2.62/2.45	2.79/2.40	-1.35	-2.19/-4.51	-4.18/-2.85	1.21
$E(\text{TO}_4)$	2.73/2.40	2.88/2.18	1.59	-3.75/-3.07	-2.85/-3.62	-1.97
$E(\text{TO}_5)$	7.39/8.31	9.28/7.34	-0.42	-5.70/-15.88	-16.06/-11.51	0.63
$E(\text{TO}_6)$	14.82/13.58	14.46/14.06	-0.97	-8.04/-5.76	-4.54/-9.32	1.14
$E(\text{TO}_7)$	0.83/2.02	2.12/0.72	4.32	-0.12/-1.35	-1.21/-0.21	-4.60
$E(\text{TO}_8)$	4.65/1.54	4.99/3.26	5.28	-2.06/-1.25	-0.80/-3.01	-4.50
$E(\text{TO}_9)$	4.06/3.45	4.05/3.41	3.18	-2.37/-3.26	-2.50/-3.09	-2.77

-
- [1] R. E. Newnham, *Properties of Materials* (Oxford University Press, 2004), ISBN 9780198520757.
- [2] R. S. Weis and T. K. Gaylord, *Applied Physics A Solids and Surfaces* **37**, 191 (1985), ISSN 0721-7250.
- [3] A. W. Warner, M. Onoe, and G. A. Coquin, *The Journal of the Acoustical Society of America* **42**, 1223 (1967), ISSN 0001-4966.
- [4] S. Sanna, S. Neufeld, M. Rüsing, G. Berth, A. Zrenner, and W. G. Schmidt, *Physical Review B* **91**, 224302 (2015), ISSN 1098-0121.